Unraveling Regulatory Feedback Mechanisms in Adult Neurogenesis Through Mathematical Modelling

Diana-Patricia Danciu[a,*], Filip Z. Klawe[a], Laura Femmer[a], Ekaterina Kostina[a,b], Ana Martin-Villalba[c], Anna Marciniak-Czochra[a,b,*]

[a] *Heidelberg University, Institute for Mathematics, Im Neuenheimer Feld 205, 69120, Heidelberg, Germany*
[b] *Interdisciplinary Center for Scientific Computing (IWR), Im Neuenheimer Feld 205, 69120, Heidelberg, Germany*
[c] *German Cancer Research Center (DKFZ), Im Neuenheimer Feld 280, 69120, Heidelberg, Germany*

SUMMARY

Adult neurogenesis is the process of generating neurons from neural stem cells in the adult brain. A comprehensive understanding of the mechanisms regulating this process is essential for developing effective interventions aimed at decelerating the decline of adult neurogenesis associated with ageing. Mathematical models provide a valuable tool for studying the dynamics of neural stem cells and their lineage, and have revealed alterations in these mechanisms during the ageing process. The present study draws upon experimental data to explore how these processes are modulated, by investigating regulatory feedbacks among neural populations through the lens of nonlinear differential equations models. Our observations indicate that the time-evolution of the neural lineage is predominantly regulated by neural stem cells, with more differentiated neural populations exerting a comparatively weaker influence. Furthermore, we illustrate the manner in which different subpopulations govern these regulations and gain insights into the impact of specific perturbations on the system.

Keywords: stem cells, adult neurogenesis, population models, mechanistic models, nonlinear ordinary differential equations, mathematical biology, optimization, model selection

1. INTRODUCTION

Adult neurogenesis is the process by which mature neurons are generated from neural stem cells (NSCs) throughout adulthood. In mammals, adult neurogenesis takes place in two main regions of the brain: the dentate gyrus (DG) of the subgranular zone in the hippocampus and the ventricular-subventricular zone (V-SVZ) located along the walls of the lateral ventricles [1–3]. In this process, NSCs transition from a quiescent to an active state, enabling self-renewal and differentiation. This results in the generation of transient amplifying progenitors (TAPs), neuroblasts (NBs), and ultimately neurons. A schematic of these transitions among the neural populations is shown in Fig. 1A. With ageing, the number of mature neurons decreases, which may lead to impaired cognitive function [4–7]. This phenomenon has been reviewed in [8, 9]. Furthermore, it has been found that the number of neural stem cells declines with age in both the V-SVZ [10–12] and the DG of the adult hippocampus [13, 14] (for reviews, see [8, 9]). As neural stem cells represent the pinnacle of the neural hierarchy and give rise to the entire neural lineage, interventions aimed at counteracting the effects of ageing could potentially have the greatest impact if they targeted stem cells. Consequently, the study of the dynamics of neural stem cell populations and their lineage is of fundamental importance for advancing our understanding of cognitive function in the context of ageing.

*Corresponding author
Email addresses: dpdanciu@math.uni-heidelberg.de (Diana-Patricia Danciu), anna.marciniak@iwr.uni-heidelberg.de (Anna Marciniak-Czochra)

As experimental studies have their limitations, mathematical methods can be employed to shed light onto processes that lead to the NSC dynamics described by the available data (Fig. 1B). As such, mechanistic mathematical models of the neural populations involving non-autonomous linear ordinary differential equations (ODEs) with time-dependent system parameters facilitated uncovering a trend in the time evolution of system parameters. Applied to the DG of the adult hippocampus [14, 15] and to the V-SVZ [12], they found that NSCs spend increasingly more time in quiescence as they progress with age. However, these models do not allow drawing conclusions regarding the regulatory mechanisms that drive this behaviour, or how different types of perturbations alter the time-course of system parameters and, as a result, of cell populations.

The current paper focuses on exploring regulatory feedbacks among cells of the neural lineage that lead to the dynamics observed. Applied to experimental data from wild-type (WT) mice, as well as complementary data from two perturbation setups, the mathematical model provides insights into the mechanisms controlling the neural lineage. These regulatory feedbacks are governed by cell-cell interactions through an elaborated network of signalling pathways. Different cells produce or interact with signalling molecules and can regulate activation, self-renewal, differentiation or proliferation. For example, it has been reported that, in zebrafish, non-glial neural progenitors similar to aNSCs and TAPs in mammals laterally inhibit the activation of quiescent NSCs by upregulating Notch ligands at the cell surface [16, 17]. Additionally, in mice it has been proposed that NSC quiescence is regulated by their immediate progeny through similar Notch paracrine signals [18], as well as diffusible ones such as the neurotransmitter GABA [19]. Notch has also been suggested to promote NSC proliferation while maintaining them in an undifferentiated state, in other words promoting self-renewal [20]. In contrast, the Ascl1 gene was found to be expressed at varying levels by proliferating lineage cells (aNSCs and TAPs) and to play a critical role in the activation of quiescent NSCs. Additionally, its inhibitor HES is expressed by quiescent cells and promotes the maintenance of quiescence. These are both tightly regulated by Notch expression, which plays an essential role in maintaining quiescent NSCs [21]. Further signals (among others) expressed in the neural lineage and involved in its regulation include bone morphogenetic protein (BMP), interferon (IFN) and Wnt. In particular, an interplay between canonical and non-canonical Wnt has been reported, with both playing a role in regulating system parameters.

A very large array of signals from the neural lineage is involved in coordinating the dynamics of NSCs and their neural lineage, with intricate interactions, whose study is extremely complex and outside the scope of this paper. These signals are further influenced by and interact with inputs from non-neural niche cells [22]. Ependymal, endothelial cells and astrocytes are some of the non-neural cell types from the neurogenic niche that contribute to regulating neurogenesis. Additionally, inflammatory signals such as Interferons (IFN) are not only involved from within the niche, but also from outside, for example through microglia or T-cells from the cerebrospinal fluid (CSF) [23]. Overall, adult neurogenesis dynamics depend on a complex web of interactions among many different signalling pathways and cell types, whose balance changes with ageing, and can be disrupted in neurological diseases [23–25]. Nevertheless, as a first step, before setting out to untangle this web, it seems advantageous to gain insights into where the driving combined signal originates and how it guides adult neurogenesis. This concept justifies the scope of our work on developing and employing nonlinear ODE models, with the aim of reducing the complexity and focusing on the basic driving actors in adult neurogenesis, their source and target.

2. RESULTS

2.1. ***Previous mathematical models suggest nonlinear feedbacks in NSC activation and self-renewal***

The main ingredients of the mechanistic model established in previous works [12, 14] correspond to the transitions among the neural lineage compartments and, in particular, among the NSC subpopulations (depicted in Fig. 1A and defined by the ODE system (1) in Fig. 1C). NSCs can exist in two exclusive states: active, which are actively cycling, and quiescent, which are not in the cell cycle. Quiescent NSCs (qNSCs) can become active at a rate r to enter the cell cycle and transition into the active compartment. An active

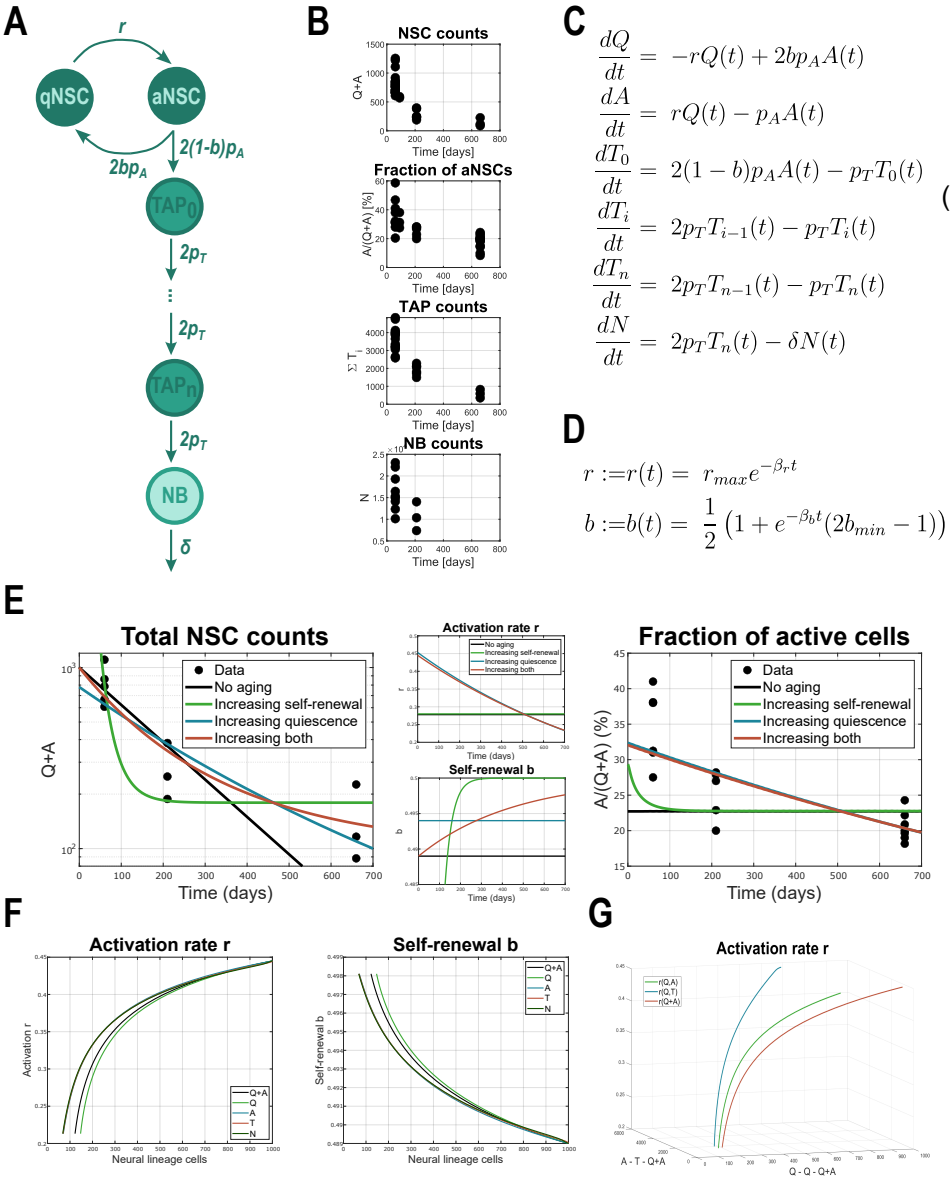

$$
\begin{aligned}
\frac{dQ}{dt} &= -rQ(t) + 2bp_A A(t) \\
\frac{dA}{dt} &= rQ(t) - p_A A(t) \\
\frac{dT_0}{dt} &= 2(1-b)p_A A(t) - p_T T_0(t) \\
\frac{dT_i}{dt} &= 2p_T T_{i-1}(t) - p_T T_i(t) \\
\frac{dT_n}{dt} &= 2p_T T_{n-1}(t) - p_T T_n(t) \\
\frac{dN}{dt} &= 2p_T T_n(t) - \delta N(t)
\end{aligned}
\tag{1}
$$

$$
\begin{aligned}
r := r(t) &= r_{max} e^{-\beta_r t} \\
b := b(t) &= \frac{1}{2}\left(1 + e^{-\beta_b t}(2b_{min} - 1)\right)
\end{aligned}
$$

Figure 1: Model description and insights on system parameters: **A.** Schematic of the transitions among neural cell types, represented in the mathematical model. **B.** Existing data from [12, 26]: total number of NSCs from the V-SVZ; fraction of active cells among label retaining cells, confirmed to be a good approximation of the fraction of active neural stem cells among all neural stem cells; total number of TAPs and total number of NBs in the V-SVZ. Each data point corresponds to one mouse. **C.** Mathematical model. System of ODEs describing the time dynamics of the neural populations depicted in A. **D.** The time-dependent functions for system parameters r and b from [12, 26]. **E.** Results of the various scenarios considered in [12] and reviewed in [27]. Plots adapted from [27]. **F.** System parameters, i.e. activation rate r and fraction of self-renewal b from the linear model plotted against values of various neural lineage populations (scaled up to 1000 cells). **G.** 3D plot of the activation rate r with respect to various combinations of neural cell subpopulations.

NSC (aNSC) can divide at a rate p_A into either two qNSCs (symmetric self-renewal) or into two TAPs (symmetric differentiation) to advance further along the differentiation path. The balance between self-renewal and differentiation is modelled via the so-called fraction of self-renewal b. This represents how many progeny of NSCs are NSCs themselves, and at the single-cell level can be thought of as a probability that the NSC self-renews. Asymmetric divisions can also be encompassed in the self-renewal parameter without any change in the model equations (an explanation can be found in [27] and [28]). TAPs are considered to perform multiple amplification steps [29] at a rate p_T before finally dividing into NBs, which can exit the compartment at a rate δ, for example by death or by migrating to another brain region. The equations (1) describing these assumptions are defined in Fig. 1C [12, 27].

Previous approaches described the changes in the system parameters r and b, by imposing certain dynamics in time through specific biologically-informed mathematical functions. The evolution of these time-dependent system parameters (depicted in Fig. 1D) was adjusted by fitting to the data and highlighted the importance of increasing quiescence. Figure 1E depicts the dynamics of the total stem cell population and of the fraction of active cells, as well as the plots of system parameters with estimated values for the scenarios in which either both are constant ("no ageing"), or one is constant and the other has a time-dynamics described in Fig. 1B ("increasing quiescence" or "increasing self-renewal"), or both are allowed to change in time ("increasing both"). Additionally, authors of [30] employed optimal control methods to examine whether control theory can predict alternative forms for the time-dependent parameters, concluding that indeed the increase in quiescence is the most important factor.

2.2. ***Nonlinear models describe system's dynamics under regulatory feedbacks***

2.2.1. Identifying the shape of feedbacks

In order to uncover regulatory feedbacks that lead to the behaviour observed in experimental data, we need to employ nonlinear ODE models. The equations (1)shown in Fig. 1C describing the model structure are used, but the system parameters r and b now depend on subpopulations of neural lineage cells, thus leading to nonlinear equations. Of note, we mention that what is referred to as "self-renewal" in biological reports is, in the case of our models, the result of an interplay between the activation rate r and the fraction of self-renewal b, mechanisms which are difficult to separate in experimental practice. Throughout this paper, we refer to the b parameter as "self-renewal", while the result of its interplay with the activation rate r is termed "effective self-renewal" [27].

So, how do the activation rate and the fraction of self-renewal depend on cell populations? By plotting the system parameters estimated from the linear models against the corresponding number of NSCs through time, we observe that r increases with the number of NSCs, whereas b decreases. In addition, experimental data show that all neural lineage cell subpopulations follow a similar decreasing trend in time (Fig.1B), and therefore the system parameters depend in a similar manner on any neural cell subpopulation. Figure 1F shows the similar dynamics of the system parameters r and b with respect to different neural subpopulations. It seems convenient to assume an activating Hill-like dependence for r and an inhibitory Hill-like dependence for b with respect to cell numbers. In other words, the system parameters can be described by equations (2), where c_i represent some cell subpopulation of the neural lineage. The parameters r_0 and b_0 govern the amplitude, whereas K and β tune the shape of the Hill functions. The same Hill-like behavior of r is observed whether c_1 and c_2 correspond to the same neural subpopulation that promotes activation, or to different neural subpopulations that regulate activation in opposing manners. This similarity can be observed in Fig. 1F and 1G, respectively.

$$\begin{aligned} r := \quad r(t) &= \frac{r_0 c_1(t)}{K + c_2(t)} \\ b := \quad b(t) &= \frac{b_0}{1 + \beta c_3(t)} \end{aligned} \tag{2}$$

2.2.2. Model selection for wild-type adult neurogenesis uncovers quiescent NSCs as the dominant promoter of activation

There exist a large number of possible combinations of the cell types c_i (2), some more plausible than others. Previous experimental studies have proposed that activation of qNSCs is promoted by aNSCs and TAPs with the aim of sustaining neurogenesis, and inhibited by NBs. In contrast, it is also reasonable to consider that the activation rate r may be inhibited by proliferating cells, such that the quiescent population is conserved when enough cells are already cycling, as was reported in zebrafish [16]. Intuitively, an activation rate that increases with the number of qNSCs is also a reasonable assumption: an abundance of qNSCs allows them to activate, as the main goal of the system is to produce neurons, not only conserve its stem cell pool. An alternative may be that all NSCs, quiescent or active, express the same driving signals for activation or self-renewal, so that the system does not distinguish the source of the feedback. As far as the regulation of self-renewal is concerned, other biological systems such as hematopoiesis [31, 32] suggest that it is inhibited by cells at the end of the differentiation spectrum (mature cells, analogous to our NBs). Such strategy seems logical if the purpose is to replenish a small NB population, since it is more efficient to first produce more stem cells that then proliferate at the same rate as before, than to proliferate faster and differentiate more [31, 33]. Self-renewal may also be inhibited by NSCs (active or quiescent), since a large number of stem cells may promote differentiation.

Function	Promoting	Inhibiting	Key signals	References
Activation of qNSCs (r)	aNSCs, TAPs, Ependymal, Astrocytes, Microglia	aNSCs, TAPs, NBs, Astrocytes, Endothelial, Microglia	Wnt, EGF, FGF2, BMPs, Notch, Shh, TGF-β, GABA	[16, 20, 23, 25, 34–37]
Self-renewal of aNSCs (b)	qNSCs, aNSCs, Astrocytes, Ependymal, Endothelial	TAPs, NBs, Astrocytes, Microglia	Notch, Wnt, EGF, FGF2, Shh, VEGF, BMPs	[20, 23, 25, 34–36]

Table 1: Overview of reported regulatory mechanisms.

Thus, we considered various scenarios corresponding to different subpopulations inserted in the c_i of our formulas (2). After performing weighted-least-squares parameter estimation to find how each scenario compares with the experimental data from WT mice, we examined the results of scenarios grouped by the regulator of self-renewal. Each panel in Figure 2 depicts the comparison among data and different hypotheses for feebacks in the activation rate of qNSCs, for self-renewal regulated by individual subpopulations (qNSCs, aNSCs, total TAPs, NBs or total NSCs). A first observation from Fig. 2 is that the subpopulation that inhibits activation is located further along the differentiation path than the one promoting the activation. Interestingly, the scenarios in which qNSCs promote activation capture the dynamics of the experimental data the best. Some hypotheses that align with the summary in Table 1 also provide an acceptable fit, but not as good as the former. Furthermore, the mathematical models clearly show that the quiescent NSCs do not have an inhibitory effect on both the activation rate and the fraction of self-renewal (Supplemental Fig. S1A). These modelling results suggest that, even though evidence of qNSCs maintaining quiescence and proliferating cells promoting activation exists (Table 1), this is not the primary mechanism involved. Instead, the balance between the combined effect of neural subpopulations and thus signalling pathways tips towards a dominant effect from qNSCs in driving activation.

In the following, we focus on a few of the best-fit scenarios, described by Equations (3)-(7). One important aspect to be noted is related to a bifurcation that appears at the point where the parameter $b_0 = 1/2$ (see mathematical analysis in STAR Methods). In particular, if $b_0 \leq 1/2$ the system only has the trivial steady state, whereas if $b > 1/2$ there exists a stable positive steady state. Depending on the regulatory feedbacks considered, upon parameter estimation, we obtain cases of good fits in which the system slowly converges to zero, and cases in which the system converges to the positive steady state (Fig. 3). Interestingly, we observe

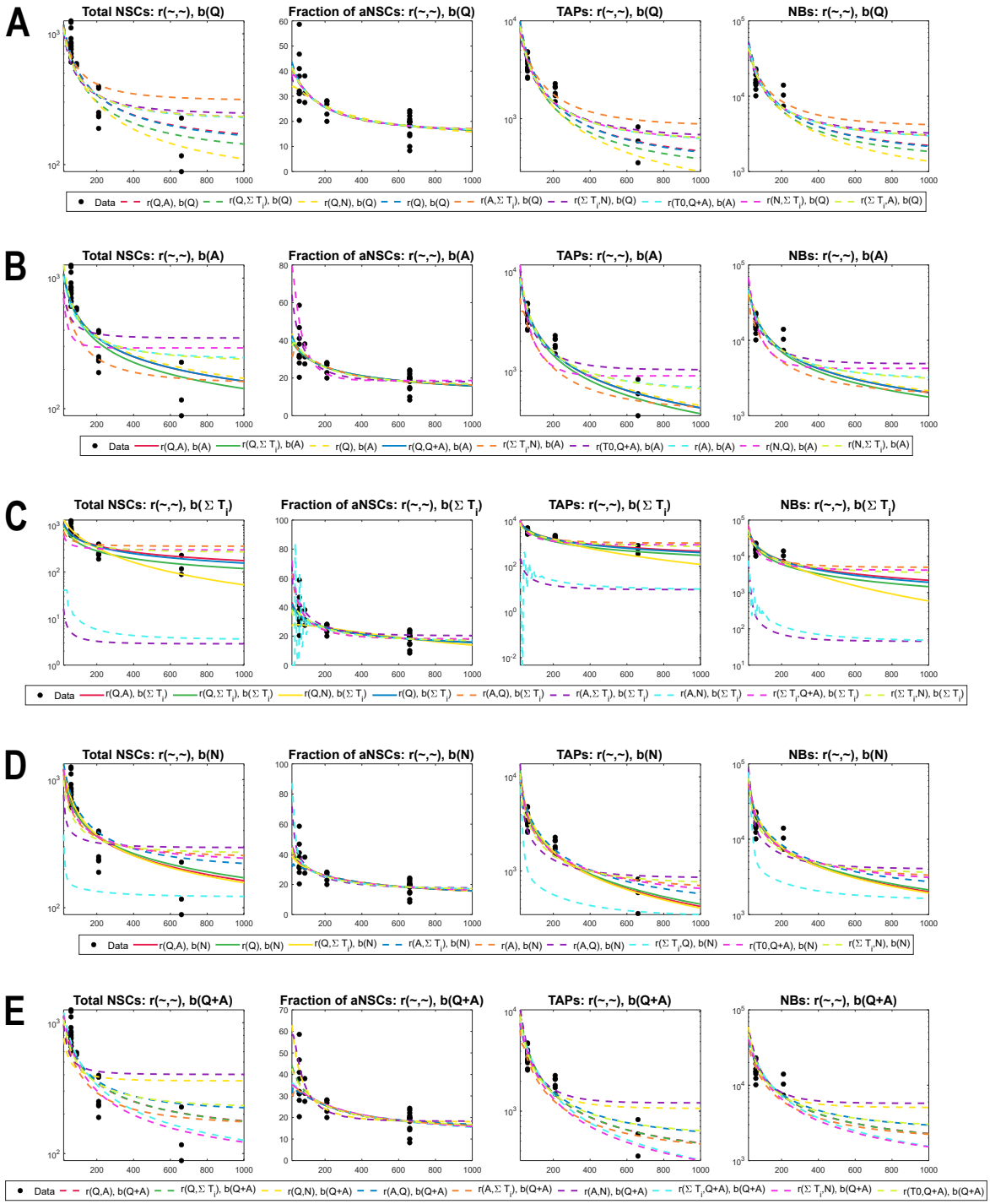

Figure 2: Comparison among various scenarios for the regulation of activation rate, grouped by the inhibitor of the self-renewal: **A.** Self-renewal inhibited by qNSC, $b(Q)$. **B.** Self-renewal inhibited by aNSC, $b(A)$. **C.** Self-renewal inhibited by TAPs, $b(\sum T_i)$. **D.** Self-renewal inhibited by NBs, $b(N)$. **E.** Self-renewal inhibited by total number of NSCs, $b(Q+A)$. As a notation rule, $r(c_1, c_2)$ corresponds to activating Hill functions (2) in which c_1 promotes (is in the numerator) and c_2 inhibits (denominator) r. Here NSC counts represent $Q(t) + A(t)$, fraction of active corresponds to $A(t)/(Q(t) + A(t))$, TAP counts is considered the sum $\sum_{i=0}^{3} T_i(t)$ and NB counts is given by $N(t)$. Full lines represent scenarios in which the estimated parameter $b_0 < 0.5$ and the system only admits the trivial equilibrium. Dotted lines correspond to scenarios in which $b_0 > 0.5$ and thus a stable positive steady state exists. X-axis represents Time, i.e. the age of mice in days. Y-axis is on log-scale in all except the plot depicting the fraction of active cells.

that the estimations for scenarios in which qNSCs are also involved in regulating self-renewal (Fig. 3A,C, Eq. (4),(6)) lead to dynamics with positive steady state. Nevertheless, since the time-span of available data is relatively short and the divergence between the two groups of curves (with $b_0 < 1/2$ and $b_0 > 1/2$) happens later, we cannot say *a priori* from a biological perspective whether we should exclude one of the two cases. It would therefore be beneficial to design experiments that might investigate this aspect, which would help with model selection. In turn, the models will be able to suggest where potential interventions should be performed based on the intended question, for example how to slow down ageing in adult neurogenesis. In order to accomplish this, we need to gain more insights into which scenario of regulatory mechanisms is more plausible than others, as each is based on different biological hypotheses and can lead to quite different biological implications.

$$r(Q,A) := \frac{r_0 Q(t)}{K + A(t)}, \qquad b(A) := \frac{b_0}{1 + \beta A(t)} \tag{3}$$

$$r(Q,A) := \frac{r_0 Q(t)}{K + A(t)}, \qquad b(Q) := \frac{b_0}{1 + \beta Q(t)} \tag{4}$$

$$r(Q,A) := \frac{r_0 Q(t)}{K + A(t)}, \qquad b(N) := \frac{b_0}{1 + \beta N(t)} \tag{5}$$

$$r(Q+A) := \frac{r_0 (Q(t) + A(t))}{K + (Q(t) + A(t))}, \qquad b(Q+A) := \frac{b_0}{1 + \beta (Q(t) + A(t))} \tag{6}$$

$$r(Q,T_0) := \frac{r_0 Q(t)}{K + T_0(t)}, \qquad b(N) := \frac{b_0}{1 + \beta N(t)} \tag{7}$$

For model comparison we resorted to computing the Akaike Information Criterion (AIC) for each of the five scenarios. The differences between the individual scores can help select the best model, and the corresponding Akaike weights tell how probable it is that the selected model is truly the best (please refer to STAR methods for details). A comparison between the AIC scores (Fig. 3D) suggests that the hypothesis in which qNSCs promote and aNSCs inhibit activation, while self-renewal is negatively regulated by qNSCs (Scenario 2, (4), "$r(Q,A), b(Q)$") is the best. However, a closer look at the rest of the scores and the associated Akaike weights points to a probability of 23.7% of this being true, followed closely by Scenario 4 (6) in which the total NSC population is involved in both promoting activation and inhibiting self-renewal ("$r(Q+A), b(Q+A)$") with a probability of 22%. The other scenarios cannot be easily discarded either, with their Akaike weights of 17.7-18.7%. Performing mathematical analysis on the five scenarios also indicates the same qualitative behaviour of the solutions (STAR Methods).

Given the similarity in the ability of the different scenarios to capture the dynamics observed in the data (Fig. 3A,C), we resorted to using more advanced optimization methods and model discrimination techniques for optimization-based model validation. Specifically, we applied the Multiple Shooting method in combination with the Gauss-Newton method [38, 39] to improve parameter estimation and model selection. These methods were used to assess whether a better fit could be obtained for some hypotheses, with the goal of distinguishing among well-fitting scenarios. Since the two parameter estimation approaches yielded nearly identical parameter values and fits, we performed F-tests to identify false models and to determine whether some models were still significantly different. When these tests were inconclusive, we used an optimal experimental design to explore the experimental conditions necessary to maximize the discrepancy among alternative scenarios. Since discriminating among these hypotheses solely based on WT data was not possible, we supplemented our investigations with data from experiments in which the biological system was perturbed. In this work, we consider two biological perturbation settings, namely 1) killing actively dividing lineage cells with the chemotherapeutic drug Temozolomide (TMZ) [12] and 2) genetically knocking out the receptors of the inflammatory signals interferon $\alpha - \gamma$ (IFNAGR KO) [26].

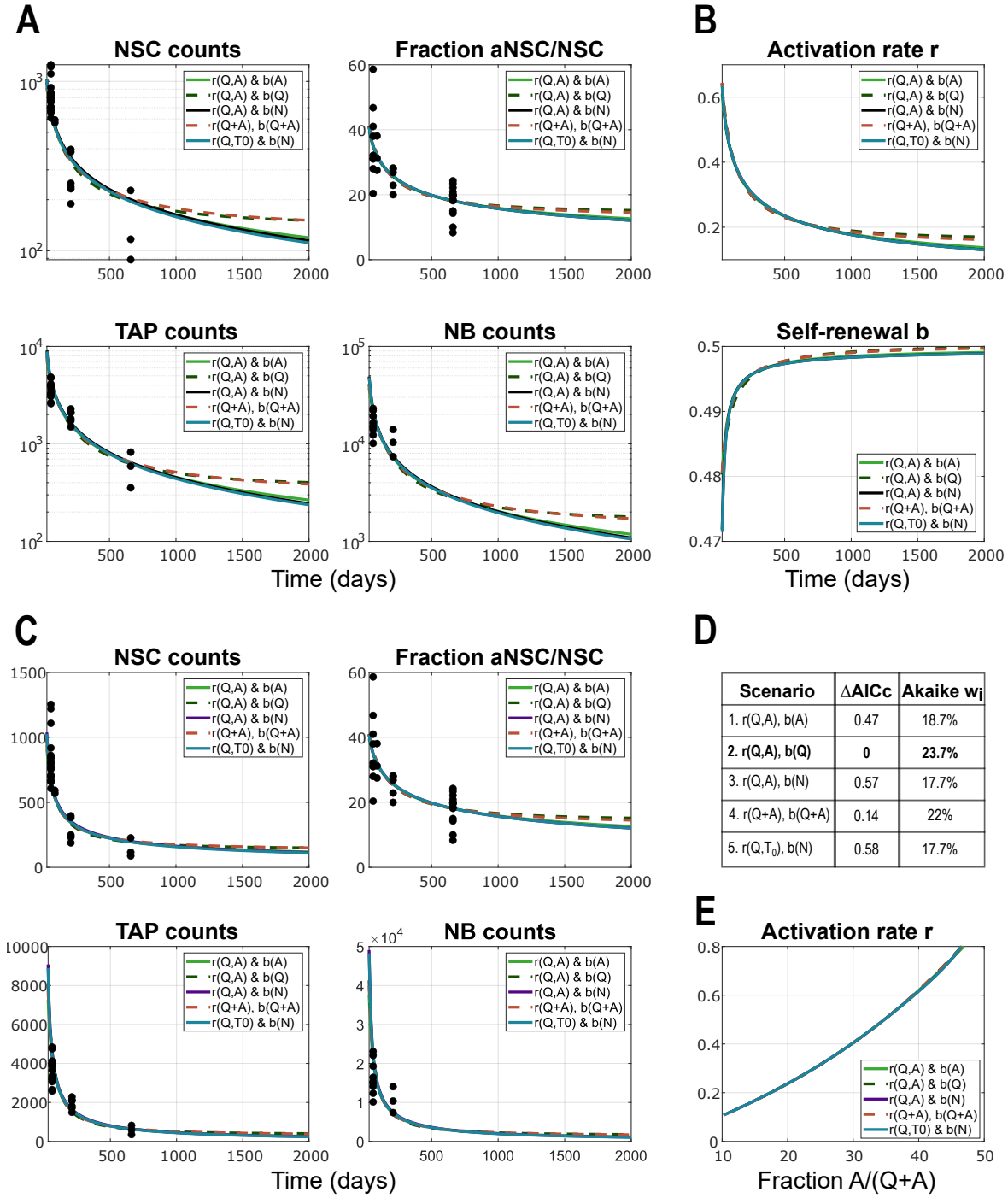

Scenario	ΔAICc	Akaike w_i
1. r(Q,A), b(A)	0.47	18.7%
2. r(Q,A), b(Q)	**0**	**23.7%**
3. r(Q,A), b(N)	0.57	17.7%
4. r(Q+A), b(Q+A)	0.14	22%
5. r(Q,T_0), b(N)	0.58	17.7%

Figure 3: Model results and comparison among the five scenarios considered, applied to data from WT mice: **A.** Results showing the dynamics of lineage cell subpopulations in time, from the parameter estimation for five different scenarios in which the system parameters are regulated by lineage cell populations. Here NSC counts represent $Q(t) + A(t)$, fraction of active corresponds to $A(t)/(Q(t) + A(t))$, TAP counts is considered the sum $\sum_{i=0}^{n} T_i(t)$ and NB counts is given by $N(t)$. The scenarios considered in these plots are described by equations (3)-(7). Continuous lines represent scenarios in which the estimated parameter $b_0 < 0.5$ and the system only admits the trivial equilibrium. Dotted lines correspond to scenarios in which $b_0 > 0.5$ and thus a stable positive steady state exists. X-axis represents Time, i.e. the age of mice in days. Y-axis is in logarithmic scale in all plots except for the one depicting the fraction of active cells. **B.** Dynamics in time of the system parameters, activation rate r and fraction of self-renewal b, from the five scenarios considered in panel A, described by equations (3)-(7). **C.** The same simulation results and data from panel A, but plotted in linear scale to emphasize the fast decrease and the heterogeneity among different mice at the various ages. **D.** Model comparison based on AICc values and their respective Akaike weights. The best model according to Akaike scores is scenario 2 (4) with $r(Q, A), b(Q)$. **E.** Activation rate r plotted against the fraction of active NSCs $A/(Q + A)$ for the five scenarios, showing an almost linear correlation. X-axis is $A/(Q + A)$, y-axis is r.

2.3. ***Model validation based on perturbation experiments***

2.3.1. Model of TMZ treatment suggests regulation of the system by the entire NSC population and describes feature selection upon injury

Temozolomide (TMZ) is a chemotherapeutic drug that can be used experimentally to kill actively proliferating cells, which in our system comprise of aNSCs (A) and TAPs (T_i). The authors of [12] performed experiments perturbing the system with TMZ in young (2-months old) and old (22-months old) mice, and recorded the recovery trend at 1, 9 and 35 days post-treatment. It was shown that in old mice the recovery is not as efficient as in young mice, so that either the numbers of proliferating cells do not recover back to the values pre-treatment, or it is much slower such that it is not seen in the first 35 days post-treatment. To gain insights into the mechanisms of recovery and the differences between young and old mice, we applied the various scenarios of the nonlinear model to the available data from the TMZ-perturbed system.

By performing the TMZ experiments *in silico* with the parameters estimated in WT data, and plotting the results we observe that the recovery is too slow compared to the data from young mice and too quick compared to that from old mice (Supplemental Fig. S1B, left). Even when trying to perform parameter estimation to fit all WT data and young and old TMZ data together with the same set of parameters (potentially allowing a slightly worse fit of WT data than before), the results are not satisfactory (Fig. S1B, right). We can thus conclude that perturbing the biological system by administering the TMZ drug changes not only the behaviour of system parameters (r and b functions) but values of individual model parameters as well.

Next, in the attempt to maintain the view as general as possible, we checked whether we can fit the data from TMZ-perturbed young and old mice with the same parameter set, but different from that estimated for WT. Intuitively, even if we keep the same model parameters in both cases, the recovery could be different due to the regulatory feedbacks among cell populations of different sizes. This is however also not the case, suggesting that not only does TMZ change the properties (parameters) of the cells but it does it differently when administered at different ages. Thus, the parameter estimation should be performed separately for young and old mice.

Proceeding step by step, we first assumed that the proliferation rates p_A and p_T were the same as in WT and not influenced by TMZ treatment, and only allowed model parameters in r and b to change. Even though the data itself could be well fitted, the solution converged to a different steady state that was high above the one from the healthy non-perturbed WT data (Supplemental Fig. S1B, middle). This seems unreasonable as it would mean that applying a chemotherapeutic drug that kills cells makes the biological system performing much better long-term. Even though this could be the case short-term, one would not expect that such a strong aggressive perturbation would prevent ageing in the long run. This result suggests that either TMZ treatment changes the parameters for a short period of time and later the system switches or transitions back to the WT parameters, or there is a different process at play, one that allows the recovery after death as well as a return to the WT behaviour after some time, whilst keeping the parameters that were estimated based on the recovery trend data. The latter was further investigated by also allowing p_A and p_T to change upon TMZ treatment.

Once again, by trying to keep the model as simple as possible and the changes due to TMZ treatment as few as possible, in order to find the essential aspect that changes upon treatment, we took a stepwise approach by allowing as few parameters as possible to differ from those from WT. We found that in young mice all parameters can remain identical as in WT apart from the proliferation rate of TAPs, p_T, which should be reduced by approximately 60%. This means that TMZ treatment affects TAPs such that they proliferate much slower than before (lengthening of cell cycle duration). Considering a heterogeneous population of proliferating cells with respect to their cell cycle length, our model parameter p_T represents a mean value of the heterogeneous proliferation rates. In this context, our results suggest that TMZ kills fast proliferating TAPs and thus select for slow dividing ones, which corresponds to the decreased value of p_T after treatment in the model. Nevertheless, properties of aNSCs seem to be unaffected by the perturbation. As far as old mice are concerned, TMZ treatment also reduced p_T (by approximately 80%), and in addition the r_0 parameter was decreased by one order of magnitude, which means that NSCs become arrested into a deeper state of quiescence, leading to a smaller mean r_0 of qNSCs. This is also in agreement with previous

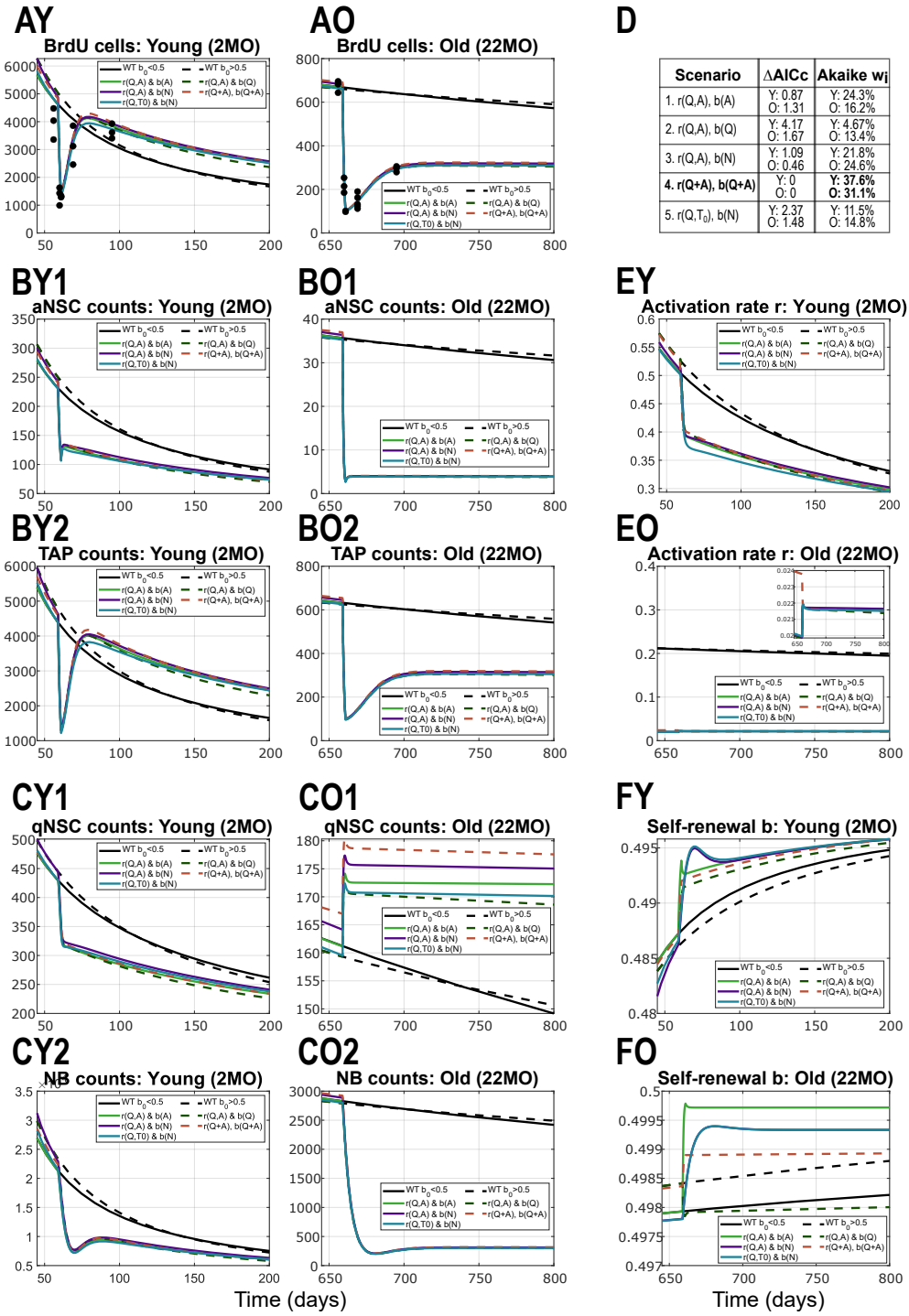

Scenario	ΔAICc	Akaike w
1. r(Q,A), b(A)	Y: 0.87 O: 1.31	Y: 24.3% O: 16.2%
2. r(Q,A), b(Q)	Y: 4.17 O: 1.67	Y: 4.67% O: 13.4%
3. r(Q,A), b(N)	Y: 1.09 O: 0.46	Y: 21.8% O: 24.6%
4. r(Q+A), b(Q+A)	Y: 0 O: 0	**Y: 37.6%** **O: 31.1%**
5. r(Q,T_0), b(N)	Y: 2.37 O: 1.48	Y: 11.5% O: 14.8%

Figure 4: Model results and comparison among the five scenarios considered, applied to data from TMZ treatment. Panels are split into young (Y) and old (O), with additional numbering. **A.** Results showing the recovery of proliferating cells (BrdU positive, consisting of aNSCs and TAPs) after TMZ treatment, in young (2MO) and old (22MO) mice. Throughout Fig. 4, black (plain and dotted) lines correspond to 2 scenarios of the WT unperturbed dynamics. More specifically, the two WT scenarios depicted are: $r(Q, A), b(A)$ (plain line) and $r(Q, A), b(Q)$ (dotted line). Plain lines (both WT and perturbed) correspond to models where $b_0 < 1/2$ (with trivial steady state), and dotted lines to scenarios in which $b_0 > 1/2$ (having a stable positive steady state). **B.** Dynamics of aNSCs (-1) and TAPs (-2), which together form the BrdU cells from panel A, in young (Y) and old (O) mice. **C.** Dynamics of the populations of qNSCs (-1) and NBs (-2) in time, as a result of TMZ intervention on BrdU cells, in young (Y) and old(O) mice. **D.** Table comparing the five scenarios based on AICc values, and their Akaike weights quantifying the individual probabilities for selection. The model in which the entire population of NSCs $(Q + A)$ regulates both r and b scores the highest (Scenario (6), "$r(Q + A), b(Q + A)$"). **E.** Activation rates r in the case of TMZ treatment compared to the WT setting, in young (Y) and old (O) mice. **F.** Fraction of self-renewal b upon TMZ treatment in comparison to the case of the unperturbed WT setting, in young (Y) and old (O) mice.

results [12] that stated that quiescent NSCs in old mice are more resistant to injury-induced activation. Additionally, we found that proliferating cells of young mice are more resistant to TMZ treatment than old mice, with a death rate of approximately 1.5-fold difference upon drug administration. With these assumptions, the model is able to recover the dynamics observed in the data (Fig. 4). We observe that some neural populations are increased post-treatment and their dynamics remain above those of the unperturbed system, while the opposite is true for others (Fig. 4B-C). In young mice, the population of TAPs after recovery is bigger than that in WT and this is due to the slower proliferation rate p_T, which eventually leads to a slower differentiation into NB and thus less exit from the neural system (Fig. 4BY2). In old mice, the dominant parameter post-treatment is r_0, the decrease of which preserves a more quiescent population and, together with the lower value of p_T, leads to a lower recovery of proliferating and differentiated cells (Fig. 4BO2).

Aiming at selecting a model scenario with the help of the additional TMZ perturbation insights, we computed the Akaike scores and weights as before. In this case, the best scenario was that in which the system parameters are both regulated by the total population of NSC (6), with Akaike weights of 37.6% for young mice and 31.1% for old mice (4D). Surprisingly, the best scenario found for the WT data scored the lowest in the case of the TMZ perturbation. Furthermore, in an attempt to better discriminate among models, we applied optimal experimental design methods to determine the age of mice to receive TMZ treatment in order to have as much discrepancy between scenarios as possible. We found that the optimal treatment age was in the interval [60,500] days old and again suggested that having available measurements of the qNSC subpopulation after treatment would increase our confidence of the model selection results, as this compartment showed the greatest differences across scenarios.

Overall, the modelling of TMZ experiments has provided interesting insights into the behaviour of the neural lineage system and the changes that appear due to treatment, and suggested that upon injury the system parameters are regulated by the entire NSC population.

2.3.2. Model of IFNAGR Knock-Out stays in agreement with insights from wild-type and describes involvement of non-neural cells in modulating activation

Proceeding further with our plan to uncover the most likely regulatory feedbacks, we decided to re-tackle the IFNAGRKO perturbation from [26]. A closer look at the data on the fractions of active NSC among all NSC (Fig. 5A, top right), suggests that in the KO mice the values grow with ageing. Additionally, we observe that generally the values of these fractions are very well, almost linearly, correlated to the activation rate (Fig. 3E), which implies that the activation rate in KO data also increases in time. Due to the way in which the time-dependent r and b functions were defined in [26] (Fig. 1D), the linear non-autonomous models were not able to capture the slight increase in the fraction of active NSC.

Using the nonlinear models with population-dependent r and b, we infer that, in order for r to increase in time, we need a slight decrease with respect to cell counts. This hints towards an inhibitory-type Hill function for r in the case of IFNAGRKO mice, similar to that for the self-renewal parameter b. Therefore, in order to allow capturing the time evolution of neural subpopulations from both WT and KO mice with the same hypothesis, we assume the following function for r whilst keeping the b function as before.

$$\begin{aligned} r := \quad r(t) &= \frac{r_1 + r_0 c_1(t)}{K + c_2(t)} \\ b := \quad b(t) &= \frac{b_0}{1 + \beta c_3(t)} \end{aligned} \tag{8}$$

As a result, our five scenarios from Eq. (3)-(7) are extended for the IFNAGRKO setting to Eq. (9)-(13).

$$r(Q,A) := \frac{r_1 + r_0 Q(t)}{K + A(t)}, \qquad b(A) := \frac{b_0}{1 + \beta A(t)} \tag{9}$$

$$r(Q,A) := \frac{r_1 + r_0 Q(t)}{K + A(t)}, \qquad b(Q) := \frac{b_0}{1 + \beta Q(t)} \tag{10}$$

$$r(Q,A) := \frac{r_1 + r_0 Q(t)}{K + A(t)}, \qquad b(N) := \frac{b_0}{1 + \beta N(t)} \tag{11}$$

$$r(Q+A) := \frac{r_1 + r_0 (Q(t) + A(t))}{K + (Q(t) + A(t))}, \qquad b(Q+A) := \frac{b_0}{1 + \beta (Q(t) + A(t))} \tag{12}$$

$$r(Q,T_0) := \frac{r_1 + r_0 Q(t)}{K + T_0(t)}, \qquad b(N) := \frac{b_0}{1 + \beta N(t)} \tag{13}$$

The simulation results for these scenarios are depicted in Fig. 5A and show that all model scenarios are very well able to capture the trend of the data. As expected based on the construction (8), both the activation rate r and the fraction of self-renewal b increase in time (Fig. 5B). Depending on the different estimated values of r parameters (i.e. r_0, r_1 and K), this definition of the r function (8) allows to capture both the decreasing fraction of active cells in WT and the increasing one in KO mice. The previous activation mechanisms modeled in the WT setting by the activating Hill-type function (2) is a particular case of the model with system parameters given by Eq. (8), with $r_1 = 0$. The insight that we can draw from the comparison between WT and IFNAGRKO results (Fig. 5C-D), is that in KO mice the activation is disregulated and consequently the self-renewal compensates (Fig. 5C-D), acting as a secondary layer of regulation, as also previously suggested [26]. Because a higher activation rate that does not decrease with ageing can lead to a fast depletion of the NSC pool, the self-renewal has a more drastic increase to counteract it. Additionally, parameter estimation suggests that the proliferation rate of TAPs is slightly higher than that in WT mice, corresponding to a cell cycle length of approximately 16h (parameter values in Supplemental Table S1).

The Akaike model comparison framework once again suggests Scenario 2 (10) as best, closely followed by Scenarios 1 (9) and 4 (12), similar to the the WT setting. Mathematical modelling thus allows us to gain new insights into the dynamics of neural lineage cells and into the dialogue bewteen neuroinflamation and adult neurogenesis, despite not clearly uncovering how the regulation is performed.

2.4. ***Interpretation in the context of signalling molecules***

The dynamics of system parameters r and b emerge from a complex network of signaling pathways operating both within and beyond the neuronal niche. By analyzing the identified dependencies of these parameters on system components, we can further investigate which cells express or bind signaling molecules that drive activation or influence the balance between self-renewal and differentiation. To achieve this, we extend the feedback model (8) to explicitly describe the signal dynamics underlying this feedback. This procedure, which can be seen as a reverse quasi-steady state reduction, is inherently challenging, as the observed feedback may result from the interplay of multiple signals. However, by modelling the regulation of activation and self-renewal by two effective signals, S_r and S_b, the temporal behaviour of the system can be captured by replacing the parameters r and b with the variables S_r and S_b, respectively, describing the effective signals, which are governed by additional differential equations (14). These equations describe the rates of production, degradation, and internalization of specific signals. Terms associated with neural cell types c_i indicate either production or consumption by the corresponding lineage cell types, depending on their sign. Positive constant terms represent signal production by non-lineage supporting cells, whereas negative linear terms describe degradation of signalling molecules. Assuming fast dynamics of the signalling molecules, the extended model can be reduced back to the nonlinear-feedback models with the Hill-type

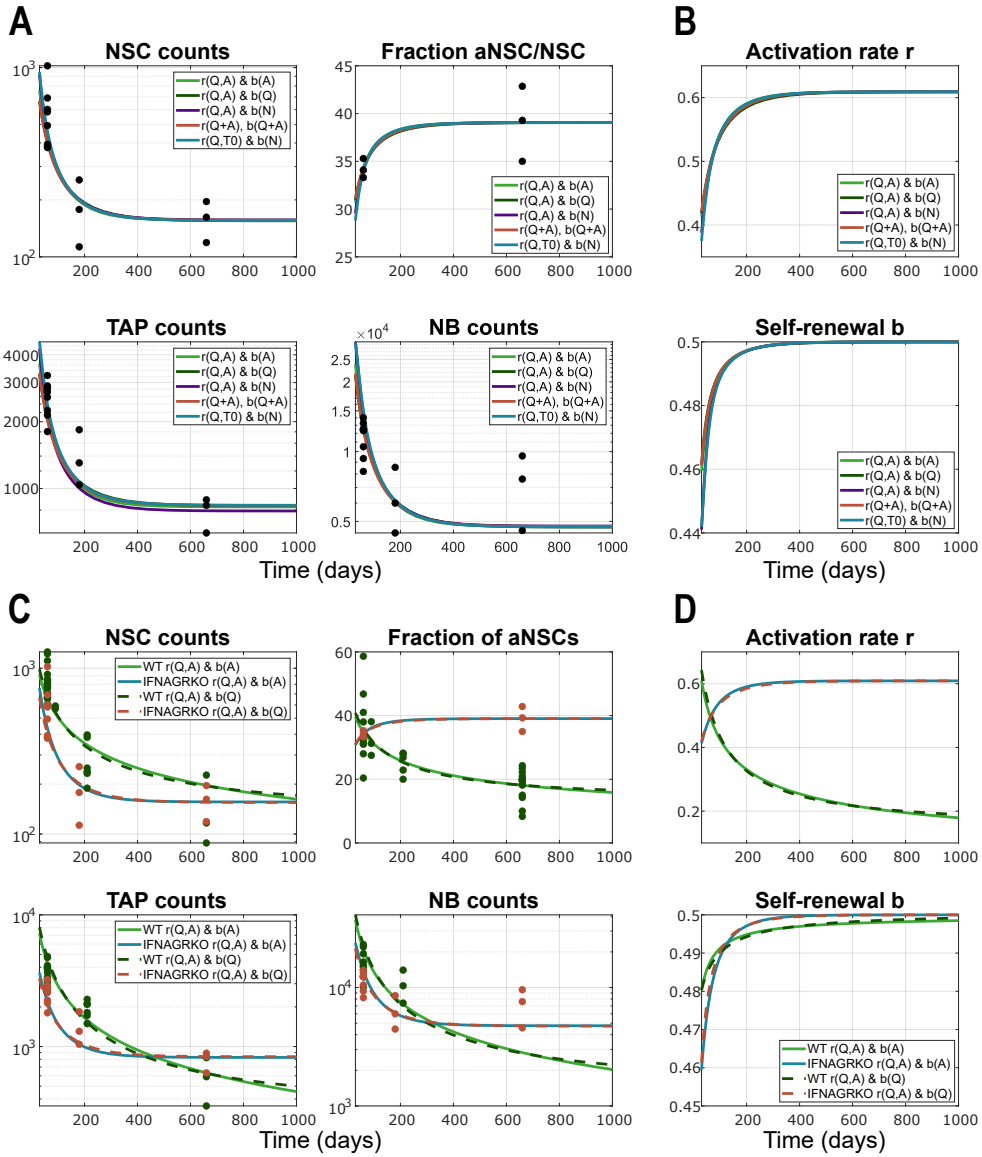

E

Scenario	ΔAICc	Akaike w_i
1. r(Q,A), b(A)	0.01	25.42%
2. r(Q,A), b(Q)	**0**	**25.57%**
3. r(Q,A), b(N)	1.05	15.06%
4. r(Q+A), b(Q+A)	0.07	24.6%
5. r(Q,T_0), b(N)	2.01	9.34%

F

Scenario	WT		TMZ		IFNAGRKO		Overall	
	ΔAICc	Akaike w_i	ΔAICc	Akaike w_i	ΔAICc	Akaike w_i	ΔAICc	Akaike w_i
1. r(Q,A), b(A)	0.46	18.76%	2.1	13.8%	0.01	25.42%	0.73	18.76%
2. r(Q,A), b(Q)	**0**	**23.71%**	2.92	9.13%	**0**	**25.57%**	**0**	**27.11%**
3. r(Q,A), b(N)	0.57	17.77%	0.81	26.32%	1.05	15.06%	1.11	15.57%
4. r(Q+A), b(Q+A)	0.14	22.04%	**0**	**39.39%**	0.07	24.6%	0.13	25.35%
5. r(Q,T_0), b(N)	0.58	17.7%	2.49	11.35%	2.01	9.34%	1.44	13.19%

Figure 5: Model results and comparison among the five scenarios considered, applied to data from IFNAGRKO mice: **A.** Simulation results showing the dynamics of lineage cell subpopulations in time, from fitting to the IFNAGRKO data, for the five different scenarios. The scenarios considered in these plots are given by equations (9)-(13). Parameter estimation finds $b_0 > 0.5$ in all five scenarios and thus the system has a stable positive steady state to which it converges. X-axis represents Time, i.e. the age of mice in days. Y-axis is in logarithmic scale in all plots except the one depicting the fraction of active cells. **B.** Dynamics in time of the system parameters, activation rate r and fraction of self-renewal b, from the five scenarios considered in panel A. **C.** Comparison between WT and IFNAGRKO fits to their respective data for two scenarios: $r(Q,A), b(A)$ (full lines, for WT $b_0 < 0.5$) and $r(Q,A), b(Q)$ (dotted lines, for WT $b_0 > 0.5$). **D.** Dynamics of the activation rate and fraction self-renewal for comparing IFNAGRKO with WT, for the scenarios considered in C. **E.** Table with AICc values for model selection and their respective Akaike weights, for the model of IFNAGRKO dynamics. **F.** Overview table with AICc scores and Akaike weights for each scenario, computed separately for WT, TMZ and IFNAGRKO, as well as combined for all settings and data together ("Overall").

functions considered before using a Tikhonov-type quasi-steady state approximation (14) [40, 41].

$$\left.\begin{aligned} \frac{dS_r}{dt} &= R_1 + R_0 c_1 - S_r - \beta_r c_2 S_r = 0 \\ \frac{dS_b}{dt} &= 1 - S_b - \beta_b c_3 S_b = 0 \end{aligned}\right\} \underset{\text{expansion}}{\overset{\text{reduction}}{\rightleftarrows}} \left\{\begin{aligned} r &:= \bar{r} S_r = \frac{\bar{r} R_1 + \bar{r} R_0 c_1}{1 + \beta_r c_2} =: \frac{r_1 + r_0 c_1}{K + c_2} \\ b &:= \bar{b} S_b = \frac{\bar{b}}{1 + \beta_b c_3} =: \frac{b_0}{1 + \beta c_3}, \end{aligned}\right. \tag{14}$$

with $r_0 = \bar{r} R_0 / \beta_r$, $r_1 = \bar{r} R_1 / \beta_r$, $K = 1/\beta_r$, $b_0 = \bar{b}$ and $\beta_b = \beta$, to recover the form and notation from before.

Consequently, this extension allows for interpreting the previously identified Hill functions in terms of specific signalling mechanisms. For WT mice, we find that the driving signal for activation is both produced and internalized by (potentially distinct) neural lineage subpopulations, corresponding to the c_1 and c_2 cell types in Eq. (2), respectively. In this context, we set $r_1 = 0$. In contrast, the dominant signal regulating the decision between self-renewal and differentiation of aNSCs is produced by non-neural supporting cells and consumed by neural lineage cells (c_3 cell type). These findings align with existing experimental evidence on autocrine and paracrine signalling. For instance, canonical Wnt is known to be secreted by astrocytes and vascular endothelial cells, taken up by neural cells, and thought to play a key role in governing aNSC self-renewal. On the other hand, by applying the nonlinear models to the experimental data from IFNAGRKO mice, we find that, the perturbed system is impaired such that the production of the activation signal by neural populations is insignificant ($r_0 \approx 0$) and non-neural supporting cells gain a much bigger impact.

Certainly, the effective signalling model (14) could be replaced by a bigger system of equations for interacting signalling molecules. For example, the activation rate may be considered as governed by two separate signals: a promoting S_{rp} and an inhibiting S_{ri} signal. Based on the previous considerations, it means the promoting S_{rp} is produced by lineage cells (c_1 as before) and is broken down by non-lineage cells or spontaneously degraded, whereas the inhibiting S_{ri} is produced by non-lineage cells and received by lineage cells (c_2). Identifying the real model underlying the feedback mechanisms would require focused experimental studies and is beyond the scope of this paper.

3. DISCUSSION

In this paper, we aimed at deciphering regulatory feedbacks acting within the neural lineage, which would be leading to the observed age-related changes in adult neurogenesis in the V-SVZ of adult mice brains. We suggested feedback mechanisms that replicate the observed dynamics and which are also plausible from a biological perspective. Although model selection did not prove entirely conclusive, we found a number of insights that can guide further experiments and investigations. First of all, we showed that the decision of a neural stem cell to self-renew or differentiate is negatively regulated by the neural lineage. From the perspective of signalling, self-renewal signalling molecules are produced by supporting cells and bound by lineage cells. Additionally, we found that the balance between activation and quiescence is mainly regulated by the neural populations, not unlikely with the involvement of two different subpopulations acting in opposing directions. The mathematical models suggested that quiescent stem cells express signalling molecules that promote activation, while another subpopulation of cells further along the differentiation path consume them to maintain quiescence. Considering the intricacy of the network of signalling interactions involved in regulating the system parameters in adult neurogenesis, it is not easy to single out specific genes, but modelling can shed light onto how and where the regulation acts.

In addition, we highlighted the risks of inference from preliminary models applied to inconclusive or insufficiently informative data without conducting a thorough and unbiased investigation, as multiple hypotheses may lead to similar results despite differing interpretations. Further, to increase the power of model selection, we used supporting data from two different perturbation experiments: the treatment with the chemotherapeutic drug TMZ, and the knock-out of the IFNAG receptors. The mathematical models applied to these complementary data uncovered compelling insights. We showed that upon TMZ treatment, the mean proliferation rate of TAPs is drastically reduced and we argue that it is likely a consequence of feature selection in a heterogeneous population: fast-proliferating TAPs are killed by TMZ and the ones

that escape are those with longer cell cycle, hence lower proliferation rate. A similar reasoning applies to old mice, where in addition the maximum activation rate is greatly reduced, leading to a surviving population of more deeply quiescent stem cells. We observed that due to slower proliferation of TAPs but a steady influx from the active NSC compartment, the total population of TAPs decays more slowly after TMZ treatment in young mice, and that this leads to a trend that lies higher than in the unperturbed system during the lifespan of mice (Fig. 4BY2). However, the populations of stem cells remain smaller than before treatment (Fig. 4BY1-BO1). Interestingly, the subpopulation with the most dissimilar behaviour across scenarios is that of quiescent NSCs (Fig. 4CY1-CO1). Although the dynamics is similar, the values of cell counts differ. Would it be possible to better select the most plausible model hypothesis if data on numbers of quiescent NSCs after treatment were available? Such data quantifying qNSCs might improve model selection assuming the heterogeneity among mice is not too high. Ideally, an additional experiment could focus on only perturbing either active NSCs or TAPs, which might help uncover whether feedback originates solely from the NSC compartments or also from more differentiated neural subpopulations.

With respect to the perturbation by knocking out IFNAG receptors, considering that data show an ascending trend of the fraction of active NSCs among all NSCs, we showed that the activation rate of quiescent NSCs increases with ageing. From the perspective of signalling, we showed that in the IFNAGRKO mice the activation signal is no longer produced by neural cells, but by supporting cells. Additionally, as the activation of quiescent NSCs is disregulated in IFNAGRKO mice, self-renewal compensates via an earlier and faster increase. As activation is a major player in the recovery after TMZ treatment in WT mice, it will be interesting to perform the TMZ experiment on IFNAGRKO mice and inspect how the neural cells behave.

Finally, in terms of selecting a model hypothesis, even though no definitive conclusion can be drawn, observations can be made from simulation results. First of all, parameter estimation for the various scenarios suggests that if qNSCs are involved in regulating the self-renewal, the system asymptotically converges to a positive steady state. The nonlinear models suggest that the driving effect for exit from quiescence most likely originates primarily from qNSCs. The table of model selection scores for the three individual settings (WT, TMZ and IFNAGRKO) together with their overall score suggests that in an uninjured setting (WT or IFNAGRKO) the main regulator of self-renewal is the qNSC subpopulation, whereas activation is primarily promoted and inhibited by qNSC and aNSC, respectively (Scenario 2, (4),(10)). In the case of a severe injury such as the treatment with TMZ, the entire NSC population is involved in regulating the system parameters to ensure a smooth recovery (Scenario 4, (6)). If we inquire how the two scenarios influence the recovery, we gather that having aNSCs contributing to regulating self-renewal (Scenario 4, (6)) leads to a faster increase in self-renewal upon their death by TMZ, than when only qNSCs are involved (Scenario 2, (4)), leading to a more efficient repopulation of the NSC pool. It is reasonable to assume that generally the two NSC subpopulations contribute with different weights in governing the system parameters, however investigating this aspect by inserting additional parameters into the models is not feasible with the available data. Additionally, our model selection results suggest that multiple neural lineage subpopulations might be involved in the regulations, with various impact, pertaining to an existing redundancy in the neural system that might ensure better adaptability. Altogether, we find that the main regulator of the dynamics of the neural lineage is the population of NSCs, whereas downstream subpopulations, if involved, have a much weaker influence.

METHODS

The current work is based on the methodology of nonlinear ordinary differential equations and combines mathematical analysis, computational simulations, parameter estimation, model selection and identifiability.

Mathematical analysis

The crucial parameter describing the dynamics of the system (1) (Fig. 1C) is b_0. It is clear that for $b_0 \leq 1/2$ it holds:

$$\frac{d(Q+A)}{dt} = \left(2\frac{b_0}{1+\beta c(t)} - 1\right) p_A A(t) \leq 0,$$

where $c(t)$ can be equal to $A(t)$, $Q(t)$, $N(t)$ or $Q(t) + A(t)$. It means that for all scenarios (3)-(7) the only steady state is a trivial one. Moreover, the solutions are asymptotically converging to it.

In the case when $b_0 > 1/2$ there exist two steady states for each model: a trivial one and a positive one. For all scenarios (3)-(7) the trivial steady state (when $b_0 > 1/2$) is unstable. The positive steady state is thus our focus in the rest of this section. We divide the models into two groups. The first comprises scenarios (3), (4) and (6), where parameters $r(\cdot)$ and $b(\cdot)$ depend only on Q and A. In these models, it is enough to consider the existence of the solution and its stability for the reduced system composed of the first two equations $(1)_{(1)}$–$(1)_{(2)}$, the results for the full model being a natural extension.

Theorem 1. *There exists a unique global solution to (1)with system parameters* (3), (4) *or* (6). *Moreover, for* $b_0 > 1/2$ *the positive steady state solution is stable.*

Proof. The functions on the right-hand side of (1) are Lipschitz-continuous for nonnegative values of the solution. Starting with nonnegative initial conditions, we obtain the local existence of unique solutions to (1) , according to the Picard–Lindelöf theorem. Using the property of the right-hand sides of (1) we obtain the positivity of the solutions.

To prove the global existence of the solution we focus on the system $(1)_{(1)}$–$(1)_{(2)}$. We will present here the results for the first scenario, i.e. (3). The reasoning in the other cases is similar. Then

$$\begin{cases} \dfrac{dQ}{dt} = -\dfrac{r_0 Q(t)}{K + A(t)} Q(t) + 2\dfrac{b_0}{1 + \beta A(t)} p_A A(t) \\ \dfrac{dA}{dt} = \dfrac{r_0 Q(t)}{K + A(t)} Q(t) - p_A A(t) \end{cases}$$

Equating the right-hand sides of the aforementioned equations to 0 we obtain two isoclines, which after transformation are equal to

$$\begin{cases} Q^2 = 2\dfrac{b_0}{1 + \beta A} \dfrac{p_A}{r_0} A(K + A) \\ Q^2 = \dfrac{p_A}{r_0} A(K + A) \end{cases}$$

It is clear that for nonnegative values of Q and A these lines have at most two intersection points: one at $(Q, A) = (0, 0)$, and a second one that occurs only when $b_0 > 1/2$. The value of the second intersection point is equal to $(\bar{Q}, \bar{A}) = \left(\sqrt{\frac{p_A}{r_0} \frac{2b_0 - 1}{\beta} (K + \frac{2b_0 - 1}{\beta})}, \frac{2b_0 - 1}{\beta}\right)$. Note that if we decrease b_0 to 1/2 from a greater value, then the second positive point goes to $(0, 0)$.

We define a domain $\mathcal{M} = \{(Q, A) \in \mathbb{R}^2 : \ Q, A \geq 0 \text{ and } Q \leq Q^*, \ A \leq A^*\}$, where $A^* > \bar{A}$ and Q^* is chosen such that $2\frac{b_0}{1+\beta A^*} \frac{p_A}{r_0} A^*(K + A^*) < (Q^*)^2 < \frac{p_A}{r_0} A^*(K + A^*)$. Then the solution with initial conditions in $\mathcal{M}$ does not escape from $\mathcal{M}$. Thus the solution is global in time.

The existence of a global unique solution for the reduced system $(1)_{(1)}$–$(1)_{(2)}$ implies the existence of a global unique solution for the full (1) system, since $Q(t)$ and $A(t)$ are bounded everywhere.

The stability of the positive steady state is a consequence of the linearization of the model in the neighbourhood of the steady state. □

We next focus on the second group of scenarios, where downstream populations are also involved in the regulation, i.e. (5) and (7).

Theorem 2. *There exists a unique global solution to (1) with* (5) *or* (7). *Moreover, for* $b_0 > 1/2$ *the positive steady state solution is stable.*

We will focus on the model with (5). Similar results can be obtained for the model with (7), but due to the higher dimensionality, we will omit the computations here.

Proof. Similarly to the proof of Theorem 1, we obtain the local existence of a unique positive solution as a consequence of Picard–Lindelöf theorem and properties of the right-hand side functions. It remains to

define a domain $\mathcal{M}$ from which the solutions cannot escape. We work with a reduced system containing only (Q, A, N), i.e. first two ODEs together with the last one in (1) further denoted (1_*). Results obtained for this model can be naturally extended to the full model (1). Moreover, for simplicity, we assume that $b_0 < 3/4$.

The invariant domain $\mathcal{M}$ for this model is a 3D polyhedral with 7 faces. The base in the (A, Q)-plane is quadrilateral. Two of their edges coincide with axes and the other two are defined by functions $Q + A = constant$ and $Q - A = constant$. The upper base is larger than the bottom one ($N = 0$). The two faces that coincide with the planes $Q = 0$ and $Q - A = const$ are pentagons. The other faces of the polyhedral are quadrilateral lying on the planes: $A = 0$, $Q + A - N = constant$ and $Q + A = constant$.

We denote $\bar{N} = \frac{2b_0-1}{\beta}$. We take an arbitrary $\underline{A}$ greater than $\bar{A} = \frac{\delta}{p_A}\bar{N}$. Moreover, $\underline{Q}$ and N^* are chosen in the following way:

$$\underline{Q} = \underline{A} + \sqrt{\left(b_0 + \frac{1}{2}\right)\frac{p}{r_0}\underline{A}(K + \underline{A})} \qquad \text{and} \qquad N^* = \frac{2p}{\delta}(\underline{Q} + \underline{A} + \bar{N}).$$

The coordinates of the vertices of the domain $\mathcal{M}$ are as follows: $\{(0,0,0), (\underline{A}+\underline{Q},0,0), (\underline{A},\underline{Q},0), (0,\underline{Q}-\underline{A},0), (0,0,N^*), (\underline{A}+\underline{Q}+\bar{N},0,N^*), (\underline{A}+\frac{\bar{N}}{2},\underline{Q}+\frac{\bar{N}}{2},N^*), (0,\underline{Q}-\underline{A},N^*), (\underline{A}+\underline{Q}+\bar{N},0,\bar{N}), (\underline{A}+\frac{\bar{N}}{2},\underline{Q}+\frac{\bar{N}}{2},\bar{N})\}$ We need to prove that solutions starting from each of the seven faces of the polyhedral domain $\mathcal{M}$ go inside the domain. We previously showed that our solutions are positive if the initial data are positive so the edges of faces that coincide with axes can be disregarded. For the rest of the faces, upon lengthy but basic calculations, we also show that the solution goes inside the domain. The results are also true for $b_0 \geq 3/4$. In this case, the angle of the trapezoidal face of the domain is modified such that it is contained in the plane $Q + A - aN$, with constant $a < 1$. For $b_0 > 1/2$, the positive steady state is stable: all three eigenvalues of the linearized system are real and negative. We find that the characteristic polynomial corresponding to the linearization matrix of the reduced system (1_*)has all coefficients negative. Thus, by the Routh-Hurwitz stability criterion we obtain that all real parts of the matrix eigenvalues are negative, and thus the steady state is stable. □

Parameter estimation

In order to see how our models are able to describe the dynamics observed in data, we performed parameter estimation. The proliferation rates $p_A = 0.95$ and $p_T = 0.81$ were kept constant, assuming a cell cycle length of 17h for aNSCs and 20h for TAPs [12]. In a first step, the parameters to be estimated comprised of $r_0, K, b_0, \beta, \delta, NSC_0$, where NSC_0 represents the total number of stem cells $(Q + A)$ at time $t = 0$. Having performed a large number of estimations the values for the last two parameters were similar most of the times, also among different scenarios. Therefore, for simplicity, we fixed $\delta = 0.19$ and $NSC_0 = 1900$. As a result, the parameters estimated comprise of r_0, K, b_0 and β for WT data. In the case of the IFNAGRKO experiments, the parameters r_1 and p_T were additionally estimated. For the young mice treated with TMZ, p_T was fitted, together with the death rate d and scaling factor ρ (see section "Model of TMZ treatment" of STAR Methods), while keeping the rest fixed. For old mice, both parameters r_0 and p_T, as well as d and ρ were fitted.

The optimization was based on weighted least squares. A cost function was defined as the sum of squared differences between the values $Q + A$, $A/(Q + A)$, $\sum_i T_i$ and N given by the ODE system at the time points at which data is available and the corresponding data values for each mouse (n total data points), divided by the variance among mice at the same time point.

$$E = \frac{1}{\sigma_i}\sum_{i=1}^{n}(y_i^{data} - y_i^{model})^2.$$

Experiment		Fixed	Estimated
WT		p_A, p_T, δ, NSC_0	r_0, K, b_0, β
TMZ	young	$r_0, K, b_0, \beta, p_A, \delta, NSC_0$	p_T, d, ρ
	old	$K, b_0, \beta, p_A, \delta, NSC_0$	r_0, p_T, d, ρ
IFNAGRKO		p_A, δ, NSC_0	$r_0, r_1, K, b_0, \beta, p_T$

Table 2: Summary of fixed and estimated parameters for each type of data.

The cost function was then minimized by using the `fmincon` routine in MathWorks MATLAB software, with the sequential quadratic programming (`'sqp'`) algorithm. The algorithm was run multiple times starting from 500 initial guesses for each model hypothesis, and the parameter set with the smallest cost function value out of the 500 multi-start points was selected.

Model selection

Model selection is performed by assigning each model a score that combines its goodness of fit with a penalty on the number of parameters to avoid overfitting. The Akaike Information Criterion, with its formulation for weighted least squares, and its correction for small samples, is one of the common scores used, defined as below[42], respectively.

$$\begin{aligned} AIC &= n \ln\left(\frac{E}{n}\right) + 2k, \\ AICc &= AIC + \frac{2k(k+1)}{n-k-1}. \end{aligned}$$

Here, k is the number of fitted parameters, n is the size of the data, and E represents the value of the minimized objective function. A smaller $AICc$ value represents a better model, in the sense of both how well it fits the data and how parsimonious it is. In model selection, the actual $AICc$ value of a model carries no real significance unless compared to those of other models. In other words, the important values to inspect are

$$\Delta_i AICc = AICc_i - AICc_{min}, \quad i \in 1, ..., M$$

representing the difference between each of the M models and the best-valued one. Despite only one model having $\Delta_i AICc = 0$, other models with very small values should also not be discarded. As there is no accurate way of deciding where the boundary between (equally-) acceptable models and bad ones should be drawn, one can resort to computing an additional metric, namely the Akaike weights. These weights can quantify how likely a model is to be the correct one, and are defined as

$$w_i = \frac{\exp(-\frac{1}{2}\Delta_i AICc)}{\sum_{i=1}^{M} \exp(-\frac{1}{2}\Delta_i AICc)}.$$

All scenarios considered in this paper have the same number of parameters and therefore we might simply compare the E-values of the minimized cost functions. However, for consistency and possible future generalization we compare the $\Delta_i AICc$ and Akaike weights w_i. The values of these scores for each hypothesis considered can be found in the Supplement.

Model of TMZ treatment

Taking into account that the data from TMZ-perturbed mice consider the numbers of proliferating cells from sections of the V-SVZ region, as opposed to cell counts from the whole region, the TMZ data need to be scaled up to compare to the WT data. This is done by fitting an additional parameter ρ that represents the scaling factor of the section-data with respect to the whole region, based on the so-called saline data recorded few days before the TMZ experiments (56 and 656 days of age in young and old mice, respectively). The scaling factor ρ thus brings the values of saline data up to the order of magnitude of WT data.

Additionally, since the death of proliferating cells is not instant upon TMZ treatment, we model an exponential decay of cell counts that considers a constant death rate d of aNSCs (A) and TAPs (T_i) due to chemotherapy during the short time-span of administering the drug. The resulting ODE system is shown in Eq. (15).

$$\begin{aligned}
\frac{dQ}{dt} &= -rQ(t) + 2bp_A A(t) \\
\frac{dA}{dt} &= rQ(t) - p_A A(t) - dA(t) \\
\frac{dT_0}{dt} &= 2(1-b)p_A A(t) - p_T T_0(t) - dT_0(t) \\
\frac{dT_i}{dt} &= 2p_T T_{i-1}(t) - p_T T_i(t) - dT_i(t) \\
\frac{dT_n}{dt} &= 2p_T T_{n-1}(t) - p_T T_n(t) - dT_n(t) \\
\frac{dN}{dt} &= 2p_T T_n(t) - \delta N(t).
\end{aligned} \tag{15}$$

The death parameter d is also estimated, when fitting the model to the experimental data. Specifically, for the period before treatment the healthy system (1) in Fig. 1C is simulated, during the treatment the model (15) is used, and after the treatment window the WT model is again used. The combined solution from these three regimes is then compared to our data points and the parameters are fitted.

Data and code availability

All original code has been deposited at Zenodo under the DOI 10.5281/zenodo.14944969 and is publicly available as of the date of publication. Any additional information required to reanalyze the data reported in this paper is available from the corresponding authors upon request.

ACKNOWLEDGMENTS

The project was supported by the European Research Council (ERC) under the European Union's Horizon 2020 research and innovation programme (synergy project PEPS, no. 101071786), and by the Deutsche Forschungsgemeinschaft (DFG) within the Collaborative Research Centre SFB1324 (B05 of AMC and B06 of AMV). The authors thank Prof. Marek Kimmel for his feedback and invaluable advice on manuscript preparation.

AUTHOR CONTRIBUTIONS

D-PD: Model development, Algorithm implementation, Interpretation of the modelling results, Manuscript preparation - original draft; FZK: Mathematical analysis, Manuscript preparation - review and editing; LF: Multiple-shooting optimization, Optimal experimental design; EK: Supervision, Multiple-shooting optimization, Optimal experimental design, Manuscript preparation - review; AM-V: Conceptualization, Supervision, Interpretation of the modelling results, Manuscript preparation - review; AM-C: Conceptualization, Supervision, Model development, Interpretation of the modelling results, Manuscript preparation - review and editing;

DECLARATION OF INTERESTS

The authors declare no competing interests.

References

[1] G. Kempermann, F. H. Gage, New nerve cells for the adult brain, Scientific American 280 (5) (1999) 48–53.

[2] J. M. Encinas, T. V. Michurina, N. Peunova, J.-H. Park, J. Tordo, D. A. Peterson, G. Fishell, A. Koulakov, G. Enikolopov, Division-coupled astrocytic differentiation and age-related depletion of neural stem cells in the adult hippocampus, Cell stem cell 8 (5) (2011) 566–579.

[3] G.-l. Ming, H. Song, Adult neurogenesis in the mammalian brain: significant answers and significant questions, Neuron 70 (4) (2011) 687–702.

[4] D. R. Seib, N. S. Corsini, K. Ellwanger, C. Plaas, A. Mateos, C. Pitzer, C. Niehrs, T. Celikel, A. Martin-Villalba, Loss of dickkopf-1 restores neurogenesis in old age and counteracts cognitive decline, Cell stem cell 12 (2) (2013) 204–214.

[5] J. C. Conover, K. L. Todd, Development and aging of a brain neural stem cell niche, Experimental gerontology 94 (2017) 9–13.

[6] G. Li, L. Fang, G. Fernández, S. J. Pleasure, The ventral hippocampus is the embryonic origin for adult neural stem cells in the dentate gyrus, Neuron 78 (4) (2013) 658–672.

[7] H. G. Kuhn, T. Toda, F. H. Gage, Adult hippocampal neurogenesis: a coming-of-age story, Journal of Neuroscience 38 (49) (2018) 10401–10410.

[8] Y. Kase, T. Shimazaki, H. Okano, Current understanding of adult neurogenesis in the mammalian brain: how does adult neurogenesis decrease with age?, Inflammation and Regeneration 40 (2020) 1–6.

[9] D. R. Seib, A. Martin-Villalba, Neurogenesis in the normal ageing hippocampus: a mini-review, Gerontology 61 (4) (2015) 327–335.

[10] F. H. Gage, Mammalian neural stem cells, Science 287 (5457) (2000) 1433–1438.

[11] V. Capilla-Gonzalez, V. Herranz-Pérez, J. M. García-Verdugo, The aged brain: genesis and fate of residual progenitor cells in the subventricular zone, Frontiers in cellular neuroscience 9 (2015) 365.

[12] G. Kalamakis, D. Brüne, S. Ravichandran, J. Bolz, W. Fan, F. Ziebell, T. Stiehl, F. Catalá-Martinez, J. Kupke, S. Zhao, E. Llorens-Bobadilla, K. Bauer, S. Limpert, B. Berger, U. Christen, P. Schmezer, J. P. Mallm, B. Berninger, S. Anders, A. del Sol, A. Marciniak-Czochra, A. Martin-Villalba, Quiescence modulates stem cell maintenance and regenerative capacity in the aging brain, Cell 176 (6) (2019) 1407–1419.e14. doi:10.1016/j.cell.2019.01.040.
URL https://linkinghub.elsevier.com/retrieve/pii/S0092867419301035

[13] S. W. Lee, G. D. Clemenson, F. H. Gage, New neurons in an aged brain, Behavioural brain research 227 (2) (2012) 497–507.

[14] F. Ziebell, S. Dehler, A. Martin-Villalba, A. Marciniak-Czochra, Revealing age-related changes of adult hippocampal neurogenesis using mathematical models, Development 145 (1) (2018). doi:10.1242/dev.153544.
URL https://dev.biologists.org/content/145/1/dev153544

[15] L. Harris, P. Rigo, T. Stiehl, Z. B. Gaber, S. H. Austin, M. del Mar Masdeu, A. Edwards, N. Urbán, A. Marciniak-Czochra, F. Guillemot, Coordinated changes in cellular behavior ensure the lifelong maintenance of the hippocampal stem cell population, Cell stem cell 28 (5) (2021) 863–876.

[16] N. Dray, L. Mancini, U. Binshtok, F. Cheysson, W. Supatto, P. Mahou, S. Bedu, S. Ortica, E. Than-Trong, M. Krecsmarik, S. Herbert, J.-B. Masson, J.-Y. Tinevez, G. Lang, E. Beaurepaire, D. Sprinzak, L. Bally-Cuif, Dynamic spatiotemporal coordination of neural stem cell fate decisions occurs through local feedback in the adult vertebrate brain 28 (8) 1457–1472.e12. doi:10.1016/j.stem.2021.03.014.
URL https://www.sciencedirect.com/science/article/pii/S193459092100120X

[17] E. Than-Trong, B. Kiani, N. Dray, S. Ortica, B. Simons, S. Rulands, A. Alunni, L. Bally-Cuif, Lineage hierarchies and stochasticity ensure the long-term maintenance of adult neural stem cells, bioRxiv (2019) 663922doi:10.1101/663922.
URL https://www.biorxiv.org/content/10.1101/663922v1

[18] D. Kawaguchi, S. Furutachi, H. Kawai, K. Hozumi, Y. Gotoh, Dll1 maintains quiescence of adult neural stem cells and segregates asymmetrically during mitosis, Nature communications 4 (1) (2013) 1880.

[19] X. Liu, Q. Wang, T. F. Haydar, A. Bordey, Nonsynaptic gaba signaling in postnatal subventricular zone controls proliferation of gfap-expressing progenitors, Nature neuroscience 8 (9) (2005) 1179–1187.

[20] C. Giachino, V. Taylor, Notching up neural stem cell homogeneity in homeostasis and disease, Frontiers in neuroscience 8 (2014) 32.

[21] R. Sueda, I. Imayoshi, Y. Harima, R. Kageyama, High hes1 expression and resultant ascl1 suppression regulate quiescent vs. active neural stem cells in the adult mouse brain, Genes & development 33 (9-10) (2019) 511–523.

[22] M. Tavazoie, L. Van der Veken, V. Silva-Vargas, M. Louissaint, L. Colonna, B. Zaidi, J. M. Garcia-Verdugo, F. Doetsch, A specialized vascular niche for adult neural stem cells, Cell stem cell 3 (3) (2008) 279–288.

[23] B. W. Dulken, M. T. Buckley, P. Navarro Negredo, N. Saligrama, R. Cayrol, D. S. Leeman, B. M. George, S. C. Boutet, K. Hebestreit, J. V. Pluvinage, et al., Single-cell analysis reveals t cell infiltration in old neurogenic niches, Nature 571 (7764) (2019) 205–210.

[24] A. M. Bond, G.-l. Ming, H. Song, Adult mammalian neural stem cells and neurogenesis: five decades later, Cell stem cell 17 (4) (2015) 385–395.

[25] H. Meng, Y. Huan, K. Zhang, X. Yi, X. Meng, E. Kang, S. Wu, W. Deng, Y. Wang, Quiescent adult neural stem cells: Developmental origin and regulatory mechanisms, Neuroscience Bulletin 40 (9) (2024) 1353–1363.
[26] D. Carvajal Ibañez, M. Skabkin, J. Hooli, S. Cerrizuela, M. Göpferich, A. Jolly, K. Volk, M. Zumwinkel, M. Bertolini, G. Figlia, et al., Interferon regulates neural stem cell function at all ages by orchestrating mtor and cell cycle, EMBO Molecular Medicine (2023) e16434.
[27] D.-P. Danciu, J. Hooli, A. Martin-Villalba, A. Marciniak-Czochra, Mathematics of neural stem cells: Linking data and processes, Cells & Development (2023) 203849.
[28] I. A. Rodriguez-Brenes, N. L. Komarova, D. Wodarz, Evolutionary dynamics of feedback escape and the development of stem-cell–driven cancers, Proceedings of the National Academy of Sciences 108 (47) (2011) 18983–18988.
[29] G. Ponti, K. Obernier, A. Alvarez-Buylla, Lineage progression from stem cells to new neurons in the adult brain ventricular-subventricular zone (2013).
[30] S. Dabelow, A. LeHanka, A. Jilkine, Distinguishing between multiple mathematical models of neural stem cell quiescence and activation during age-related neural stem cell decline in neurogenesis, Mathematical Biosciences 346 (2022) 108807.
[31] A. Marciniak-Czochra, T. Stiehl, A. D. Ho, W. Jäger, W. Wagner, Modeling of asymmetric cell division in hematopoietic stem cells—regulation of self-renewal is essential for efficient repopulation, Stem cells and development 18 (3) (2009) 377–386.
[32] T. Stiehl, A. Marciniak-Czochra, Stem cell self-renewal in regeneration and cancer: Insights from mathematical modeling, Current Opinion in Systems Biology 5 (2017) 112–120. doi:10.1016/j.coisb.2017.09.006.
URL http://www.sciencedirect.com/science/article/pii/S2452310017301245
[33] T. Stiehl, A. Marciniak-Czochra, Stem cell self-renewal in regeneration and cancer: insights from mathematical modeling, Current Opinion in Systems Biology 5 (2017) 112–120.
[34] D. A. Lim, A. Alvarez-Buylla, The adult ventricular–subventricular zone (v-svz) and olfactory bulb (ob) neurogenesis, Cold Spring Harbor perspectives in biology 8 (5) (2016) a018820.
[35] R. Faigle, H. Song, Signaling mechanisms regulating adult neural stem cells and neurogenesis, Biochimica et Biophysica Acta (BBA)-General Subjects 1830 (2) (2013) 2435–2448.
[36] K. Obernier, A. Alvarez-Buylla, Neural stem cells: origin, heterogeneity and regulation in the adult mammalian brain, Development 146 (4) (2019) dev156059.
[37] E. Llorens-Bobadilla, S. Zhao, A. Baser, G. Saiz-Castro, K. Zwadlo, A. Martin-Villalba, Single-cell transcriptomics reveals a population of dormant neural stem cells that become activated upon brain injury, Cell Stem Cell 17 (3) (2015) 329–340. doi:10.1016/j.stem.2015.07.002.
URL http://www.sciencedirect.com/science/article/pii/S193459091500301X
[38] H. G. Bock, Numerical treatment of inverse problems in chemical reaction kinetics, in: Modelling of Chemical Reaction Systems: Proceedings of an International Workshop, Heidelberg, Fed. Rep. of Germany, September 1–5, 1980, Springer, 1981, pp. 102–125.
[39] H. G. Bock, E. Kostina, J. P. Schlöder, Direct multiple shooting and generalized gauss-newton method for parameter estimation problems in ode models, in: Multiple Shooting and Time Domain Decomposition Methods: MuS-TDD, Heidelberg, May 6-8, 2013, Springer, 2015, pp. 1–34.
[40] W. S. Loud, Differential equations. by an tikhonov, ab vasil'eva and ag sveshnikov, The American Mathematical Monthly 94 (3) (1987) 308–310.
[41] A. Marciniak-Czochra, A. Mikelić, T. Stiehl, Renormalization group second-order approximation for singularly perturbed nonlinear ordinary differential equations, Mathematical Methods in the Applied Sciences 41 (14) (2018) 5691–5710.
[42] H. T. Banks, M. L. Joyner, Aic under the framework of least squares estimation, Applied Mathematics Letters 74 (2017) 33–45.

Table S1: Parameter values for the five scenarios

Scenario	r0_wt	K_wt	b0_wt	beta_wt	r0_ifnko	r1_ifnko	K_ifnko	b0_ifnko	beta_ifnko	pT_TMZ_y	d_TMZ_y	rho_TMZ_y	r0_TMZ_o	pT_TMZ_o	d_TMZ_o	rho_TMZ_o
r(Q,A), b(A)	2.3583	1774.3	0.49994	0.00011306	221.03	0	301.94	0.51611	0.0005284	0.44291	0.66398	39.128	0.22357	0.18146	0.96003	39.128
r(Q,A), b(Q)	2.4376	1808.5	0.50557	9.0097E-05	191.17	0.0030268	253.77	0.51106	0.0002341	0.44968	0.71346	38.744	0.22986	0.18068	0.95958	38.744
r(Q,A), b(N)	2.2707	1735.5	0.49952	1.195E-06	191.91	0.019638	256.84	0.51306	5.4708E-06	0.45263	0.67971	39.985	0.21505	0.18101	0.95967	39.985
r(Q+A), b(Q+A)	1.5015	1252.3	0.50355	5.0994E-05	315.52	0.21125	415.88	0.51317	0.00016873	0.43631	0.66279	40.516	0.16984	0.18093	0.96058	40.516
r(Q,T0), b(N)	2.4994	1857.9	0.49952	1.2342E-06	227.09	0	316.7	0.51284	5.4203E-06	0.44646	0.68597	38.926	0.23758	0.18032	0.95958	38.926

Table S2: Akaike scores for each scenario

Scenario	AICc	ΔAICc	Akaike weights
r(Q,A), b(A)	-1427.537237	0.749237896	23.0871787
r(Q,A), b(Q)	-1428.286475	0	33.57884908
r(Q,A), b(N)	-1424.658985	3.627490398	5.474774993
r(Q+A), b(Q+A)	-1428.148514	0.137960875	31.34064882
r(Q,T0), b(N)	-1425.007986	3.278489326	6.518548405

Supplemental Figures

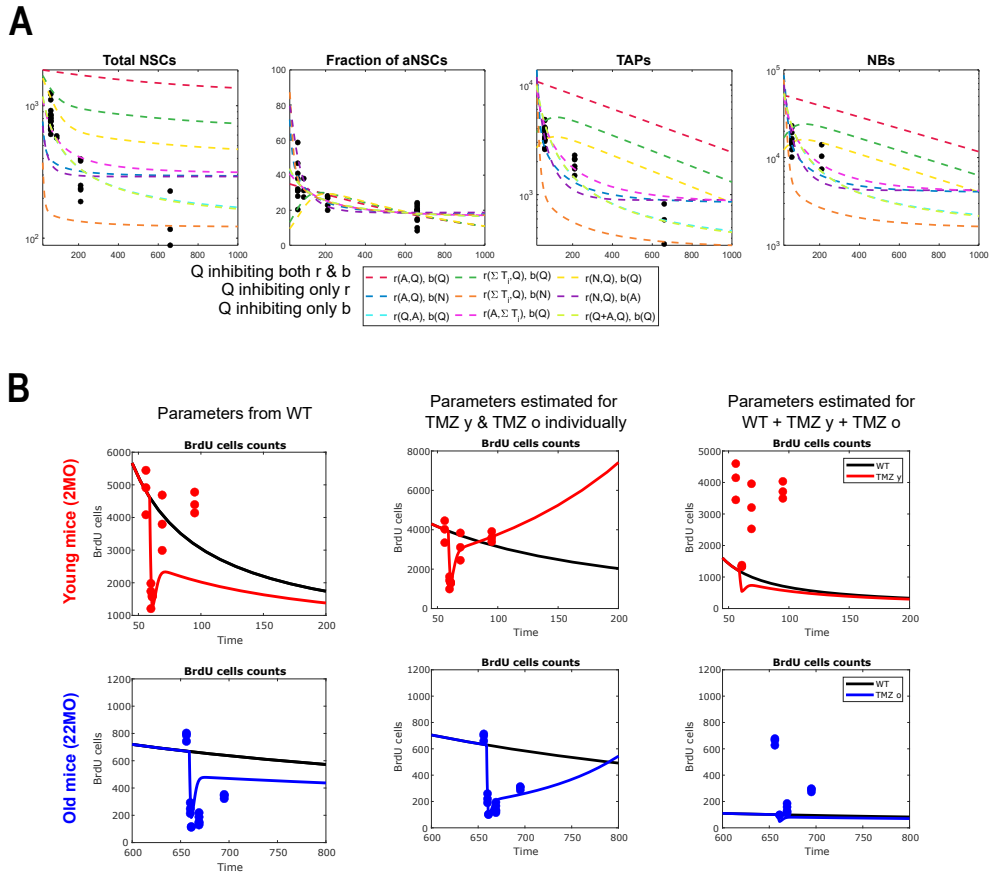

Figure S1: Examples of bad fits to WT and TMZ data: **A.** Scenarios in which either Q inhibits both r and b, only r or only b. The estimated $b_0 > 1/2$ for all these, so the solutions converge to the positive steady state. **B.** Results of *in silico* TMZ treatment with parameters estimated for WT (left); all parameters estimated individually for young and old TMZ data (middle); and parameters estimated for fitting all data together (from WT, TMZ young and TMZ old mice). Red represents TMZ-treated young mice, blue corresponds to TMZ-treated old mice and black to WT mice. The scenario shown is that with system parameters $r(Q, A)$ and $b(A)$ (3), but the same behaviour is seen for all of the five best-fit hypotheses (3)-(7).